Photocurrent enhancement of chemically synthesized Ag nanoparticle-embedded $BiFeO_3$ thin films

Rika Maruyama[1], Wataru Sakamoto[1]*, Isamu Yuitoo[2], Teruaki Takeuchi[2], Koichiro Hayashi[1], and Toshinobu Yogo[1]

[1]*Division of Materials Research, Institute of Materials and Systems for Sustainability, Nagoya University, Nagoya 464-8603, Japan*

[2]*Research Organization for Nano and Life Innovation, Waseda University, Shinjuku, Tokyo 162-0041, Japan*

*E-mail: sakamoto@imass.nagoya-u.ac.jp

$BiFeO_3$ and Ag nanoparticle-embedded $BiFeO_3$ thin films were prepared on $Pt/TiO_x/SiO_2/Si$ and MgO(100) substrates using colloidal silver and $BiFeO_3$ metal-organic precursor solutions. Colloidal silver solution was prepared by a chemical reductive method using $NaBH_4$ as a reductant. The prepared Ag nanoparticles exhibited characteristic optical absorption properties based on their surface plasmon resonance related to particle size. The synthesized $BiFeO_3$ and Ag nanoparticle/$BiFeO_3$ thin films demonstrated rapid on/off responses of photocurrent to visible light. The Ag nanoparticle-incorporated $BiFeO_3$ film exhibited a 2-4-fold higher photocurrent than the $BiFeO_3$ film. Optical and ferroelectric properties did not change markedly even when Ag nanoparticles were embedded in the $BiFeO_3$ thin film within the quantities of this study. Furthermore, in the Ag nanoparticle/$BiFeO_3$ composite structure, Ag nanoparticles were introduced in the near-metallic state with maintained their nanometer size. In the Ag nanoparticle-embedded $BiFeO_3$ film, photoinduced charge separation and transport of photoexcited carriers were enhanced by the surface plasmon effect of nanosized Ag particles as well as the internal bias electric field existed in the narrow-bandgap $BiFeO_3$ thin film.

1. Introduction

The photovoltaic effect in ferroelectric substances has been known and about half a century passed since it was discovered in $BaTiO_3$.[1] Now, environmental power generation attracts great attention as a technique of converting various environmental energies into electrical energy. In particular, environmental micropower generation is regarded as important according to the progress of low-consumption electronic devices.[2] In such a situation, multiferroic $BiFeO_3$,[3,4] which has a relatively small bandgap energy (2.1–2.8 eV)[5-8] in a wide variety of ferroelectric oxides, has recently been gathering much interest because of its photovoltaic effect and switchable photocurrent under visible light irradiation. These characteristic photoinduced responses are significant appealing points of $BiFeO_3$-based ferroelectric compounds.[9-16] The origin of these properties is closely related to the optical properties (including their narrow bandgap), ferroelectric polarization state, and defect formation in $BiFeO_3$. Therefore, narrow-bandgap ferroelectrics were expected to be promising candidates for realizing a novel energy-harvesting device utilizing photoelectric conversion.

To apply functional materials such as photovoltaic $BiFeO_3$ in high-integrated electronic devices (for example, microsized sensor systems), thin-film processing becomes more important in various fields. There are several fabrication methods for thin films of functional materials. Among them, the solution coating technique has advantages, such as its applicability to versatile shaping (including the fabrication of composite materials), simple and easy process, and low equipment cost because special apparatuses such as high-vacuum systems are not required.

Ferroelectric $BiFeO_3$-based photoresponsive materials, however, have serious problems such as poor photoelectric conversion properties, especially low photocurrent,

under visible light irradiation.[9,17,18] The photoinduced properties of $BiFeO_3$-based materials are usually not sufficient for desired applications. In several trials, the substitution of various ions in the Bi and Fe sites of $BiFeO_3$,[19-22] and the fabrication of noble metal-based nanoparticles/ferroelectric composites[23] or layered thin films with transparent oxide materials[10,24,25] (for example, indium-tin oxide) have been investigated with the aim of improving their photoinduced properties. The authors have already reported that the internal bias electric field caused by the space charge distribution in the unpoled $BiFeO_3$ film has an important effect on photoinduced electrical properties.[21,26] Moreover, the enhancement of photocurrent and photovoltaic properties by forming a p-n heterojunction between Al-doped ZnO (n-type) and $BiFeO_3$ (p-type) semiconducting films through the control of the internal bias field in the layered film has been reported.[27]

On the other hand, in photocatalysts, promoting the effective separation of photogenerated electron–hole pairs is the key to achieving a high photocatalytic activity of semiconductors. Therefore, nanosized noble metals (Ag, Au, Pt, etc.) have been frequently used to improve the photoelectrochemical performances of photocatalysts by enhancing the charge separation using their characteristic optical properties.[28-31] In several noble metal-based materials, Ag nanoparticles exhibit a particularly superior characteristic called “surface plasmon resonance” in the visible wavelength range.[32] In this work, Ag nanoparticle-embedded $BiFeO_3$ films are synthesized to improve photoelectric current properties. In this case, the localized surface plasmon resonance induced by the collective oscillations of surface electrons on Ag nanoparticles enhances the visible light harvesting of $BiFeO_3$ and promotes electron–hole separation.[33,34] As a result, Ag nanoparticle/$BiFeO_3$ composite films are expected to show higher visible

light absorption capability and an enhanced charge separation than $BiFeO_3$ films and achieve higher photocurrent generation. Therefore, narrow-bandgap ferroelectric $BiFeO_3$ and Ag nanoparticle composite thin films were fabricated by a chemical coating process using colloidal silver and $BiFeO_3$ metal-organic precursor solution. Then, the effects of Ag nanoparticle (as a surface plasmon excitation agent) incorporation on the optical, ferroelectric, photocurrent, and photovoltaic properties, in addition to the crystallographic phase and microstructure of the resultant thin films, were studied.

2. Experimental procedure

2.1 Preparation of colloidal silver solution

To fabricate Ag nanoparticle-embedded $BiFeO_3$ thin films, a Ag nanoparticle dispersion liquid (0.25 mM) is prepared by chemical reductive method.[35] In this case, 2-methoxyethanol is selected as a solvent because of the wettability of the colloidal silver solution on the surface of a $BiFeO_3$ film. Polyvinylpyrrolidone (PVP, Kishida Chemical; molecular weight, 40,000) is selected as a dispersant and mixed with 2-methoxyethanol yielding a 0.1 mM solution (22.75 ml). $AgNO_3$ (Kishida Chemical, 99.8%) is also dissolved in 2-methoxyethanol yielding a 5 mM solution (1.25 ml). These two solutions are mixed at room temperature. Then, a $NaBH_4$ (Tokyo Chemical Industry, >95.0%)-10 mM 2-methoxyethanol solution (1.0 ml) is added gradually drop by drop with cooling in an ice bath at 5^{o}C. The entire addition took about 3 h. After dripping, this solution is stirred at room temperature for 15 min and then put in a cool and dark space for 12-18 h without stirring. A clear yellow colloidal silver solution (25 ml) is obtained. This colloidal silver is stable at room temperature and is stored in a brown-colored vial for several weeks or months.

2.2 Preparation of $BiFeO_3$ precursor solution

$Bi(O^tC_5H_{11})_3$ and $Fe(OC_2H_5)_3$ (Kojundo Chemical) are used as starting materials for preparing the $BiFeO_3$ precursor solution. All procedures are conducted in a dry N_2 atmosphere because the starting metal alkoxides are extremely sensitive to moisture. 2-Methoxyethanol (used as a solvent) is dried using molecular sieves and distilled prior to use. The required amounts of the starting metal alkoxides corresponding to the composition $BiFeO_3$ with 5 mol% excess Bi are dissolved in absolute 2-methoxyethanol. In this case, the 5 mol% excess $Bi(O^tC_5H_{11})_3$ is added to compensate for the loss due to Bi volatilization during the heat treatment of the precursor films. The solution is then heated to 90 °C for 18 h, yielding a 0.2 M $BiFeO_3$ precursor solution.

2.3 Fabrication of $BiFeO_3$ and Ag nanoparticle-embedded $BiFeO_3$ thin films

A $BiFeO_3$ precursor film is fabricated from the $BiFeO_3$ precursor solution by spin coating at 2500 rpm for 30 s onto $Pt/TiO_x/SiO_2/Si$ and MgO(100) substrates. A Ag nanoparticle layer in the $BiFeO_3$ film is also prepared from the colloidal silver solution by spin coating onto $BiFeO_3/Pt/TiO_x/SiO_2/Si$, MgO(100) and $BiFeO_3$/MgO(100). The $BiFeO_3$ precursor film is dried at 150 °C for 5 min, then calcined at 400 °C for 1 h (heating rate: 5°C/min) in O_2 flow using a conventional tube furnace (10°C/min). After 5 drying and calcining cycles, the film is crystallized at 600°C for 30 min in O_2 flow by rapid thermal annealing (180 °C/min). This process is repeated twice (10 coatings in total), yielding a crystalline $BiFeO_3$ thin film. The $BiFeO_3$ film without Ag nanoparticles is hereafter referred to as “BF”. To fabricate a $BiFeO_3$/Ag nanoparticle/$BiFeO_3$ (abbreviated as “BAB”: one Ag nanoparticle layer composite) film,

a Ag nanoparticle layer is fabricated from the colloidal silver solution by spin coating on $BiFeO_3/Pt/TiO_x/SiO_2/Si$. In the BAB film, Ag nanoparticle coating is performed after crystallization of 5 coating layers of $BiFeO_3$. In this case, the Ag nanoparticle layer is prepared in the middle of the $BiFeO_3$ film. Furthermore, in a $BiFeO_3$/Ag nanoparticle/$BiFeO_3$/Ag nanoparticle/$BiFeO_3$ film (hereafter, "BABAB" film), two Ag nanoparticle layers at the position divides a $BiFeO_3$ film thickness into three parts. In the BABAB film, Ag nanoparticle coatings are deposited on the surface of $BiFeO_3$ film after 3 and 7 coating of $BiFeO_3$. Schematic illustrations (detailed structures) of the BF, BAB, and BABAB thin films synthesized in this study are shown in Fig. 1. The thicknesses of the resultant BF, BAB, and BABAB films are approximately 500-550 nm.

2.4 Characterization of Ag nanoparticle, $BiFeO_3$, and Ag nanoparticle-embedded $BiFeO_3$ thin films

The crystallographic phase of the resulting $BiFeO_3$ (BF) and Ag nanoparticle-embedded BF thin films is confirmed by X-ray diffraction (XRD; Rigaku Smart Lab–DPK) analysis using monochromated Cu Kα radiation. The optical transmittance spectra of the Ag nanoparticle, BF, BAB, and BABAB thin films on MgO(100) are measured using an ultraviolet (UV)-visible spectrometer (JASCO V-570). The sizes and shapes of the prepared Ag nanoparticles are observed using a transmission electron microscopy (TEM; Hitachi H-800) system operated at 200 kV. The microstructure of the composite thin films is also characterized by field-emission scanning electron microscopy (FE-SEM; JEOL JSM-7500FA) and scanning transmission electron microscopy (STEM; Hitachi STEM HD-2700) systems operated

at 200 kV. To observe a STEM image, the Ag nanoparticle-embedded BF thin film is machined using a focused ion beam apparatus (FIB; Hitachi FIBSEM NB5000) operated at 40 kV. Chemical analysis of the Ag nanoparticles incorporated BF films are performed by energy dispersive X-ray spectroscopy (EDX; AMETEK EDAX Octane T Ultra W 100 mm^2 Silicon Drift Detector). Top Pt electrodes of 0.2 mm diameter are deposited by direct current (DC) sputtering on the surfaces of the films on the $Pt/TiO_x/SiO_2/Si$ substrates, followed by annealing at 400 °C for 1 h. The current density (J) vs voltage (V) or time (s) characteristics of the films are evaluated using an electrometer/high-resistance meter (Keithley Instruments 6517A). The ferroelectric properties are measured using a ferroelectric test system (Toyo FCE-1) at 1 kHz. The electrical properties of the thin films at room temperature and 83 K are measured in a wafer cryostat (Sanwa WM-363-1) under vacuum (1.0 Pa). Current density measurements under dark conditions and visible- (400–700 nm, 90 klx), blue- (450 nm, 1 mW/cm^2), green- (530 nm, 1.38 mW/cm^2), and red- (650 nm, 1.5 mW/cm^2) light irradiation using a xenon light source (Asahi Spectra LAX-C100, 60 W) with several appropriate optical filters (short-pass, long-pass, and band-pass filters) are also performed for the BF and Ag nanoparticle-embedded BF thin films.

3. Results and discussion

3.1 Synthesis and characterization of Ag nanoparticles

A stable colloidal silver solution is prepared by the chemical reductive method using $AgNO_3$ as a starting material, $NaBH_4$ as a reducing agent, PVP as a dispersant, and 2-methoxyethanol as a solvent. Ag nanoparticles are deposited on the transparent MgO(100) substrate or $BiFeO_3$ film surface by spin coating. Figure 2(a) shows a TEM

image of Ag nanoparticles in colloidal silver, and the size distribution is estimated to be 2-10 nm. Figure 2(b) shows the UV-visible absorption spectrum of the Ag nanoparticles on a MgO(100) substrate after coating and drying. A weak characteristic broad absorption peak is observed in the visible wavelength region of 390-480 nm. This is due to the characteristic surface plasmon absorption of Ag nanoparticles synthesized in this study. The distinctive yellow color of colloidal silver is related to the size of dispersed Ag nanoparticle. The surface plasmon resonance produces a peak near 420 nm with a full width at half maximum (FWHM) of approximately 50 nm. In general, as the particles become larger, the surface plasmon absorption peak shifts to longer wavelengths and broadens. The size of the nanoparticles in colloidal silver affects this behavior and the result here is consistent with those in a previous report.[36)]

3.2 Fabrication and properties of $BiFeO_3$ and Ag nanoparticle-embedded $BiFeO_3$ thin films

Figure 3 shows the XRD patterns of the BF, BAB, and BABAB thin films fabricated on the Pt/TiO_x/SiO_2/Si substrates. The diffraction profiles of the films in Fig. 3 contain the diffraction peaks (except for the diffraction peaks attributable to the substrate) identified to correspond to rhombohedral perovskite $BiFeO_3$, although a slight preferential orientation is observed for the films. Owing to the excess Bi (5 mol%) in the precursor solutions, the compositions of the resultant crystallized BF films are determined by electron probe microanalysis, and the composition ratio of Bi/Fe is confirmed to be approximately 1.0 after crystallization. In Fig. 3, no peaks corresponding to additional or intermediate phases are observed. Under the present processing condition with the amount of embedded Ag nanoparticle being very small, as

described later, no diffraction lines of Ag are observed in Fig. 3.

The optical properties of BF, BAB, and BABAB films prepared on MgO(100) are evaluated using a UV-visible spectrometer. In these case, MgO(100) is used as a substrate because of its high transparency over a wide wavelength region ($\lambda > 200$ nm). Figure 4 shows the UV-visible transmission spectra of BF and Ag nanoparticle/BF films. From the UV-visible transmittance spectra, these thin films are observed to absorb light at wavelengths of less than 600 nm, indicating visible light absorption in the range of 400-600 nm, and the absorption edges are not greatly affected by the Ag nanoparticle incorporation. These transmittance spectral curves of the BF-based films overlap with the surface plasmon absorption wavelengths of Ag nanoparticles. In addition, absorption edges exist in the visible light region, and each bandgap that is calculated from each spectrum on the basis of the $(\alpha h\nu)^{1/2}$ vs photon energy ($h\nu$) relationships (Tauc plots) is approximately 2.2 eV. In this case, the band structure of $BiFeO_3$ is considered to be representative of an indirect bandgap as reported by Neaton *et al*.[37] The calculated bandgap value is consistent with that introduced in a previous report on the estimation for an indirect-energy-gap semiconductor.[6,21] Although the energy bandgap is smaller than that of the $BiFeO_3$ films prepared by physical vapor deposition,[7] this smaller bandgap in the present work indicates the possibility of utilizing more of the visible light spectrum. However, clarification of the reason for the reduced bandgap energy is left as a future study.

Figure 5(a) shows a surface FE-SEM image of Ag nanoparticles deposited on $BiFeO_3/Pt/TiO_x/SiO_2/Si$ after heat treatment at 600^{o}C. The film surface is relatively porous morphology. A SEM micrograph reveals that the amount of Ag nanoparticle on the BF film is very small. Furthermore, in Ag nanoparticles on the BF film, grain growth

and increase in the size of nanoparticles to approximately 10-20 nm are observed. Furthermore, cross-sectional annular dark field (ADF)-STEM observation of the BABAB composite film and Ag Lα EDX signal mapping are also performed to confirm the structure of the Ag nanoparticles embedded in the BF film. The composite film and Pt bottom electrode are observed on a STEM image [Fig. 5(b)], and the BABAB film thickness is found to be approximately 550 nm. In addition, a bright part is recognized on an EDX element mapping image in Fig. 5(c). In this image, the bright part of the Ag mapping image above the upper side of the composite film corresponds the signal of Ar Kα and Ar Kβ contained in the protective layer for machining of the composite film. The EDX spectrum of the circled part in Fig. 5(c) is extracted and shown in Fig. 5(d). A signal of Ag Lα is clearly seen in this spectrum. Furthermore, the intensity of the signal of O Kα is confirmed to be lower than that measured at the BF film part without Ag nanoparticles, in relation to the signal intensity ratio of Ag Lα to O Kα. It is considered that the nanoparticles in the composite films are in the near-metallic state. From the results in Fig. 5, Ag nanoparticle-embedded BF thin films comprising $BiFeO_3$ and Ag nanoparticles are successfully synthesized by optimizing the processing conditions. However, Fig. 5(a) reveals that the density of embedded Ag nanoparticle is estimated to be a few hundred per 1 μm^2. This low particle density in the BF films might make the observation of Ag nanoparticles in a cross-sectional STEM image very difficult, as shown in Fig. 5(b).

Figure 6 shows the polarization (*P)* vs electric field (*E*) hysteresis loops of BF [Fig. 6(a)], BAB [Fig. 6(b)], and BABAB [Fig. 6(c)] thin films on Pt/TiO_x/SiO_2/Si substrates. The measurement is performed at 83 K and 1 kHz under dark conditions. The BF and Ag nanoparticle/BF composite thin films fabricated in this study show poor ferroelectric

properties at room temperature because of their low electrical resistivity at high applied fields. Well-shaped *P–E* loops, however, are obtained for both films at a low temperature of 83 K, as shown in Fig. 6. This is due to the attained high electrical resistivity, which enables us to confirm the potential ferroelectricity of the BF and Ag/BF composite thin films. As shown in Fig. 6, although the remanent polarization ($2P_r$) of the Ag nanoparticle/BF composite thin films (approximately 190 μC/cm^2) is slightly higher than that of the BF film (approximately 170 μC/cm^2), the coercive field ($2E_c$) of the Ag nanoparticle/BF composite films (approximately 650 kV/cm) is consistent with that of the BF film (approximately 700 kV/cm). Also, the *P*-*E* loops are asymmetrical both for positive (from bottom to top of the electrode) and negative (from top to bottom of the electrode) applied fields. Since both the top and bottom electrodes used in this study are platinum, the asymmetrical behavior described above is attributed to the internal bias fields in the BF and Ag nanoparticle/BF composite films. The ferroelectric properties of the BF and Ag nanoparticle/BF films do not change markedly. Also, the leakage current properties of the synthesized films, regardless of the existence of Ag nanoparticle layer, measured at room temperature are confirmed to show quite a small difference over wide applied field range.

3.3 Photoinduced electrical properties of $BiFeO_3$ and Ag nanoparticle-embedded $BiFeO_3$ thin films

Figure 7 shows the photocurrent densities of the BF [Fig. 7(a)], BAB [Fig. 7(b)], and BABAB [Fig. 7(c)] thin films on Pt/TiO_x/SiO_2/Si substrates with and without white light (400–700 nm, 90 klx) irradiation. The short-circuit current densities are measured every second. In this figure, “on” corresponds to irradiation with white light and “off”

corresponds to dark conditions. Changes in current densities occur rapidly upon white light irradiation. The measurement is performed at room temperature on the as-prepared BF, BAB, and BABAB thin films without any poling treatment. In this figure, a gradual increase in photoinduced current under white light irradiation is considered to be due to the resistivity change related to the increase in the temperature of the thin film surface. The authors have already reported that the BF film absorbs the light of this wavelength and that the estimated bandgap is approximately in the range of 2.1-2.2 eV.[21,26] In these films, the photocurrent direction is from the top electrode to the bottom electrode. In the case of the BF film, from the direction of the electric current, the internal bias electric field[9,11,12,21,25,38] caused by the space charge distribution in the BF film (especially that of oxygen vacancies) is considered to strongly affect the generation of photocurrent.[38] This internal bias field is formed by the cation and anion defects generated during the heat treatment of the BF thin films, because the bismuth and oxygen vacancies seem to be ununiformly distributed across the film depth. As can be seen in Figs. 7(b) and 7(c), the magnitude of the photocurrent density of the Ag nanoparticle/BF composite films increase approximately by two-fold in BAB and four-fold in BABAB films compared with the BF film without Ag nanoparticles. The improvement of photoinduced properties is achieved with the electrical properties of the BF thin film maintained.

The dependence of irradiation light wavelength on the photoelectric current behavior related to the contribution of the surface plasmon effect is also evaluated. Figure 8 shows the photocurrent densities of the BF [Fig. 8(a)] and BABAB [Fig. 8(b)] thin films on Pt/TiO_x/SiO_2/Si substrates with and without blue (450 nm) or green (530 nm) or red (650 nm) light irradiation. The measurement is also performed at room temperature on the as-prepared BF and BABAB thin films without any poling treatment.

Unlike white light, relatively constant photocurrent under illumination is due to the suppression of the increase in the temperature of the thin film surface related to the power of light of each wavelength. The photocurrent density increases in the BABAB composite film, especially under blue light irradiation, as shown in Fig. 8(b). On the other hand, the magnitude of the photocurrent density under green or red light irradiation does not change compared with that of the BF film. As for this result, the increase in the photocurrent of the Ag nanoparticle-embedded BF film supports the contribution of surface plasmon absorption of Ag nanoparticles in the blue light wavelength region. In addition, this result is reasonable because the absorption wavelength of the Ag nanoparticles is close to the wavelength of irradiation light (blue light), although a slight grain growth occurs after heat treatment, as shown in Fig. 3. This leads to the observed increase in the magnitude of photoinduced current caused by the formation of the Ag nanoparticle/BF composite film. However, comparison considering the absorption factor of each wavelength for the films is a future work.

The effect of the introduction of Ag nanoparticle on photovoltaic properties is also characterized by the same measurement as reported by the authors.[21,27)] The open circuit voltage (V_{OC}) estimated from the *J*–*V* curve under the on and off conditions of blue light (450 nm) does not change approximately 0.30 V (BF film) for the film with the BABAB structure (0.31 V). Therefore, Ag nanoparticles incorporated in the BF film do not affect the photovoltage (V_{OC}). Also, the maximum power density estimated from these data also improves to approximately 0.1 μW/cm^2 for the BABAB composite film from approximately 0.02 μW/cm^2 for the BF film. For the BF and Ag nanoparticle/BF thin films currently under discussion, the self-bias electric field formed in the BF film is the main reason for the generation of the photovoltaic effect from the as-prepared thin films

without any poling treatment.

Yang *et al*. have already reported the effect of AgO nanoparticle incorporation on the photoinduced electrical properties of $Pb(Zr,Ti)O_3$ thin films.[23] However, photocurrent enhancement by incorporating Ag nanoparticles in BF-based thin films has never been reported. The results in this study reveal that the improvement of photocurrent properties caused by the surface plasmon resonance can be combined with the bulk photoinduced effect of the ferroelectric thin film. By the surface plasmon resonance of the Ag nanoparticles embedded in the BF thin film, the near-field light is enhanced around the nanoparticles. That is, light in the wavelength range of 400-450 nm is strengthened near the surface of Ag nanoparticles. The localized surface plasmon resonance on Ag nanoparticles may enhance the visible light harvesting of $BiFeO_3$ and effectively induces electron-hole separation.[34] Photoexcited carriers move to the electrodes in accordance with the internal electric field in the BF thin film. As a result, the Ag nanoparticle/BF composite film has higher visible light absorption capability and an enhanced charge separation than the BF film and thus exhibits higher-photocurrent generation.

In the ferroelectric photovoltaic effect, the poling state of crystals should be considered. Therefore, investigating the effects of poling on the switchable photoinduced electrical properties and further investigations of the condition at the interface between the BF and Ag nanoparticle, and the processing conditions including the amount and size dependences of Ag nanoparticle are also important for further improvement of the photoinduced electrical properties. In particular, investigation of the control of the surface plasmon absorption wavelength of Ag nanoparticle (particle size control) and quantity of embedded Ag nanoparticle in the BF film is strongly required to

further increase photoelectric current as well as to clarify the mechanism. These investigations are now in progress to enhance photoelectric conversion properties of the BF thin films.

4. Conclusions

Polycrystalline $BiFeO_3$ (BF) and Ag nanoparticle-embedded BF thin films are synthesized by a chemical process and demonstrate a photocurrent under visible light irradiation with rapid responses. Ag nanoparticles (2-10 nm) dispersed in liquid are successfully prepared by chemical reductive method using PVP as a dispersant and $NaBH_4$ as a reduction agent. The Ag nanoparticles with diameters of 10–20 nm are embedded in the BF film after crystallization at 600^{o}C. The estimated bandgaps of BF and Ag nanoparticle/BF films are approximately 2.2 eV. Within the quantity of embedded Ag nanoparticle in this study, the magnitude of photocurrent of the Ag nanoparticle/BF composite film on Pt/TiO_x/SiO_2/Si is approximately 2-4-fold larger than that of the BF film. In Ag nanoparticle/BF composite films, the internal bias electric field combined with the surface plasmon resonance effect of Ag nanoparticles in the BF films is an important key to the enhancement of photoinduced electrical current with the electrical properties of the BF film maintained. Further optimization of the amount and size of the embedded Ag nanoparticle will effectively lead to the enhancement of photocurrent generation. The Ag nanoparticle-embedded BF composite thin film developed in this study opens a window for the development of novel energy-harvesting devices based on photoelectric conversion utilizing narrow-bandgap ferroelectric materials.

Acknowledgement

This work was supported by joint research projects on “Advanced Materials Development and Integration of Novel Structured Metallic and Inorganic Materials” and “Development Base on Creation of Life Innovation Materials for Interdisciplinary and International Researcher Development” (Inter-University Collaboration of 6 Research Institutes) from the Ministry of Education, Culture, Sports, Science and Technology, Japan.

References

1. A. G. Chynoweth, Phys. Rev. **102**, 705 (1956).
2. R. J. M. Vullers, R. V. Schaijk, I. Doms, C. V. Hoof, and R. Mertens, Solid-State Electron. **53**, 684 (2009).
3. J. Wang, J. B. Neaton, H. Zheng, V. Nagarajan, S. B. Ogale, B. Liu, D. Viehland, V. Vaithyanathan, D. G. Schlom, U. V. Waghmare, N. A. Spaldin, K. M. Rabe, M. Wuttig, and R. Ramesh, Science **299**, 1719 (2003).
4. G. Catalan and J. F. Scott, Adv. Mater. **21**, 2463 (2009).
5. F. Gao, Y. Yuan, K. F. Wang, X. Y. Chen, F. Chen, J.-M. Liu, and Z. F. Ren, Appl. Phys. Lett. **89**, 102506 (2006).
6. F. Gao, X. Chen, K. Yin, S. Dong, Z. Ren, F. Yuan, T. Yu, Z. Zou, and J.-M. Liu, Adv. Mater. **19**, 2889 (2007).
7. J. F. Ihlefeld, N. J. Podraza, Z. K. Liu, R. C. Rai, X. Xu, T. Heeg, Y. B. Chen, J. Li, R. W. Collins, J. L. Musfeldt, X. Q. Pan, J. Schubert, R. Ramesh, and D. G. Schlom, Appl. Phys. Lett. **92**, 142908 (2008).

8. A. Kumar, R. C. Rai, N. J. Podraza, S. Denev, M. Ramirez, Y.-H. Chu, L. W. Martin, J. Ihlefeld, T. Heeg, J. Schubert, D. G. Schlom, J. Orenstein, R. Ramesh, R. W. Collins, J. L. Musfeldt, and V. Gopalan, Appl. Phys. Lett. **92**, 121915 (2008).
9. T. Choi, S. Lee, Y. J. Choi, V. Kiryukhin, and S.-W. Cheong, Science **324**, 63 (2009).
10. S. Y. Yang, L. W. Martin, S. J. Byrnes, T. E. Conry, S. R. Basu, D. Paran, L. Reichertz, J. Ihlefeld, C. Adamo, A. Melville, Y.-H. Chu, C.-H. Yang, J. L. Musfeldt, D. G. Schlom, J. W. Ager, and R. Ramesh, Appl. Phys. Lett. **95**, 062909 (2009).
11. W. Ji, K. Yao, and Y. C. Liang, Adv. Mater. **22**, 1763 (2010).
12. S. Y. Yang, J. Seidal, S. J. Byrnes, P. Sharfer, C.-H. Yang, M. D. Rossell, P. Yu, Y.-H. Chu, J. F. Scott, J. W. Ager, L. W. Martin, and R. Ramesh, Nat. Nanotechnol. **5**, 143 (2010).
13. D. Lee, S. H. Baek, T. H. Kim, J. G. Yoon, C. M. Folkman, C. B. Eom, and T. W. Noh, Phys. Rev. B **84**, 125305 (2011).
14. Y. Yuan, Z. Xiao, B. Yang, and J. Huang, J. Mater. Chem. A **2**, 6027 (2014).
15. S. Nakashima, T. Uchida, D. Nakayama, H. Fujisawa, M. Kobune, and M. Shimizu, Jpn. J. Appl. Phys. **53**, 09PA16 (2014).
16. S. Nakashima, K. Takayama, T. Uchida, H. Fujisawa, and M. Shimizu, Jpn. J. Appl. Phys. **54**, 10NA16 (2015).
17. W. Ji, K. Yao, and Y. C. Liang, Adv. Mater. **22**, 1763 (2010).
18. M. Alexe and D. Hesse, Nat. Commun. **2**, 256 (2011).
19. Y. Ukai, S. Yamazaki, T. Kawae, and A. Morimoto, Jpn. J. Appl. Phys. **51**, 09LE10 (2012).
20. G. Khan, R. Das, N. Mukherjee, and K. Mandal, Phys. Status Solidi: Rapid Res. Lett. **6**, 312 (2012).

21. K. Yoshida, W. Sakamoto, M. Moriya, and T. Yogo, Jpn. J. Appl. Phys. **53**, 09PA17 (2014).

22. V. S. Puli, D. K. Pradhan, R. K. Katiyar, I. Coondoo, N. Panwar, P. Misra, D. B. Chrisey, J. F. Scott, and R. S. Katiyar, J. Phys. D **47**, 075502 (2014).

23. X. Yang, X. Su, M. Shen, F. Zheng, Y. Xin, L. Zhang, M. Hua, Y. Chen, and V. G. Harris, Adv. Mater. **24**, 1202 (2012).

24. B. Chen, M. Li, Y. Liu, Z. Zuo, F. Zhuge, Q.-F. Zhan, and R.-W. Li, Nanotechnology **22**, 195201 (2011).

25. W. Dong, Y. Guo, B. Guo, H. Liu, H. Li, and H. Liu, Mater. Lett. **91**, 359 (2013).

26. N. Makino, W. Sakamoto, K. Yoshida, M. Moriya, and T. Yogo, Ferroelectrics **453**, 20 (2013).

27. T. Katayama, W. Sakamoto, I. Yuitoo, T. Takeuchi, K. Hayashi, and T. Yogo, Jpn. J. Appl. Phys. **54**, 10NA05 (2015).

28. Y. Zhao, B. Yang, J. Xu, Z. Fu, M. Wu, and F. Li, Thin Solid Films **520**, 3515 (2012).

29. S. Li, J. M. Zhang, M. G. Kibria, Z. Mi, M. Chaker, D. L. Ma, R. Nechache, and F. Rosei, Chem. Commun. **49**, 5856 (2013).

30. R. Adhikari, S. Malla, G. Gyawali, T. Sekino, and S. W. Lee, Mater. Res. Bull. **48**, 3367 (2013).

31. L. J. Di, H. Yang, G. Hu, T. Xian, J. Y. Ma, J. L. Jiang, R. S. Li, and Z. Q. Wei, J. Mater. Sci. Mater. Electron. **25**, 2463 (2014).

32. P. Mulvaney, Langmuir **12**, 788 (1996).

33. Z. Zhang, W. Wang, E. Gao, S. Sun, and L. Zhang, J. Phys. Chem. C **116**, 25898 (2012).

34. H. Lu, Z. Du, J. Wang, and Y. Liu, Sol-Gel Sci. Technol. **76**, 50 (2015).

35. S. D. Solomon, M. Bahadory, A. V. Jeyarajasingam, S. A. Rutkowsky, C. Boritz, and L. Mulfinger, J. Chem. Edu. **84**, 322 (2007).

36. I. Pastoriza-Santos and L. M. Liz-Marzán, Langmuir **18**, 2888 (2002).

37. J. B. Neaton, C. Ederer, U. V. Waghmare, N. A. Spaldin, and K. M. Rabe, Phys. Rev. B **71**, 014113 (2005).

38. R. L. Gao, H. W. Yang, Y. S. Chen, J. R. Sun, Y. G. Zhao, and B. G. Shen, Appl. Phys. Lett. **104**, 031906 (2014).

Figure captions

Fig. 1 Schematic illustrations of prepared (a) $BiFeO_3$ (BF), (b) $BiFeO_3$/Ag nanoparticle/$BiFeO_3$ (BAB), and (c) $BiFeO_3$/Ag nanoparticle/$BiFeO_3$/Ag nanoparticle/$BiFeO_3$ (BABAB) thin films on Pt/TiO_x/SiO_2/Si substrates.

Fig. 2 (a) TEM image of Ag nanoparticles prepared by chemical reductive method and (b) UV-visible optical transmittance spectrum of Ag particles on MgO(100) substrate.

Fig. 3 (Color online) XRD profiles of (a) BF, (b) BAB, and (c) BABAB thin films prepared on Pt/TiO_x/SiO_2/Si substrates.

Fig. 4 (Color online) UV-visible optical transmittance spectra of (a) BF, (b) BAB, and (c) BABAB thin films prepared on MgO(100) substrates.

Fig. 5 (Color online) (a) FE-SEM surface image of Ag nanoparticle-coated BF thin film after heat treatment at 600^{o}C, (b) Cross-sectional ADF-STEM image of BABAB thin film on Pt/TiO_x/SiO_2/Si substrate, (c) Ag Lα EDX signal mapping of BABAB film for selected area in (b), and (d) EDX spectrum of the circled area of BABAB film in (c).

Fig. 6 (Color online) *P–E* hysteresis loops (measured at 83 K and 1 kHz under dark conditions) of (a) BF, (b) BAB, and (c) BABAB thin films prepared on Pt/TiO_x/SiO_2/Si substrates.

Fig. 7 (Color online) Zero-bias photoelectric current properties (measured at room temperature) of (a) BF, (b) BAB, and (c) BABAB thin films prepared on Pt/TiO_x/SiO_2/Si substrates as a function of time under dark (off) and white light (λ =400–700 nm, 90 klx) irradiation (on) conditions.

Fig. 8 (Color online) Zero-bias photoinduced current density of (a) BF and (b) BABAB thin films prepared on Pt/TiO_x/SiO_2/Si substrates as a function of time with blue light (λ = 450 nm), green light (λ = 530 nm), and red light (λ = 650 nm) on or off.

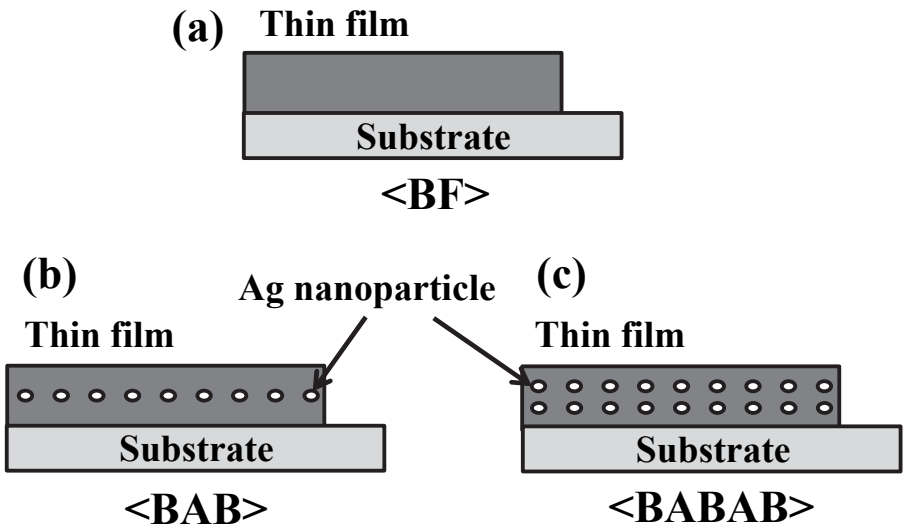

Fig. 1 Schematic illustrations of prepared (a) $BiFeO_3$ (BF), (b) $BiFeO_3$/Ag nanoparticle/$BiFeO_3$ (BAB), and (c) $BiFeO_3$/Ag nanoparticle/$BiFeO_3$/Ag nanoparticle/$BiFeO_3$ (BABAB) thin films on Pt/TiO_x/SiO_2/Si substrates.

Fig. 1 Maruyama *et al*.

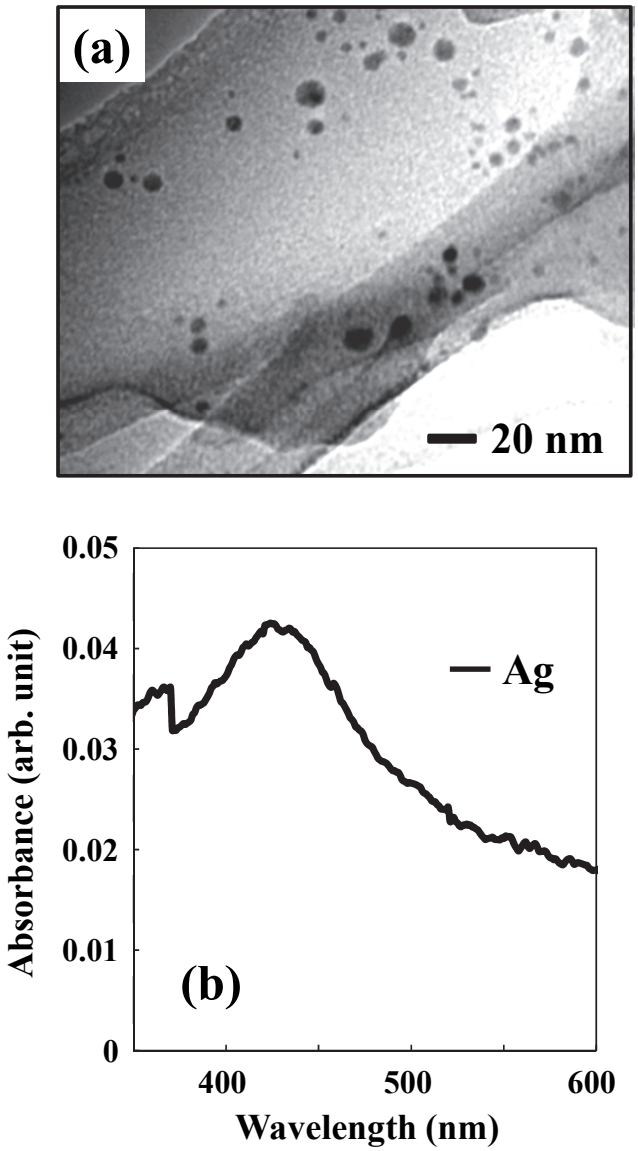

Fig. 2 (a) TEM image of Ag nanoparticles prepared by chemical reductive method and (b) UV-visible optical transmittance spectrum of Ag particles on MgO(100) substrate.

Fig. 2 Maruyama *et al*.

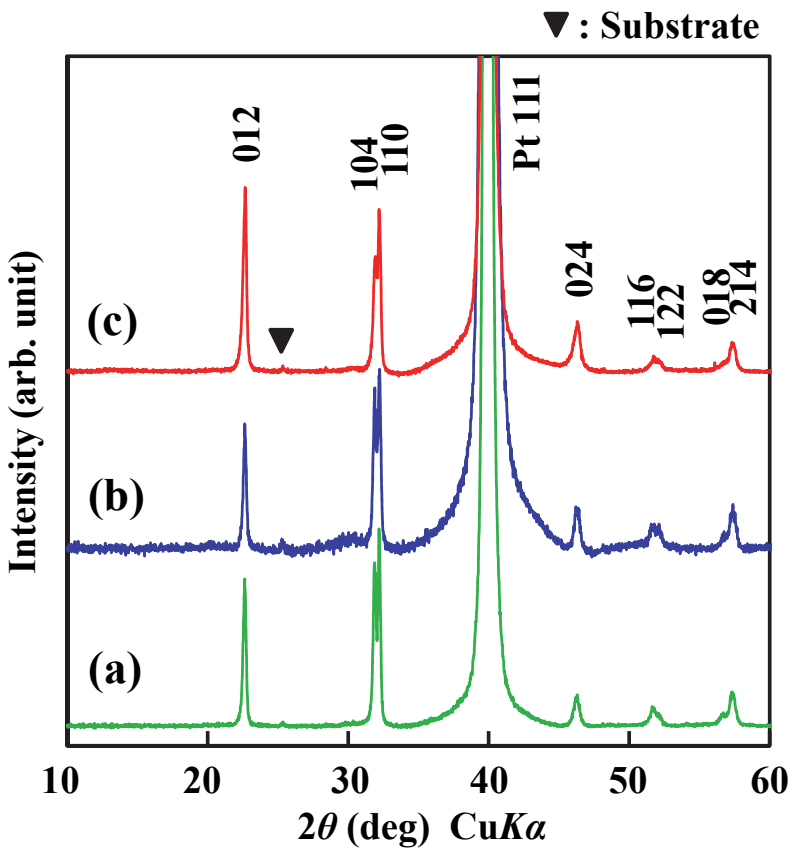

Fig. 3 (Color online) XRD profiles of (a) BF, (b) BAB, and (c) BABAB thin films prepared on Pt/TiO_x/SiO_2/Si substrates.

Fig. 3 Maruyama *et al*.

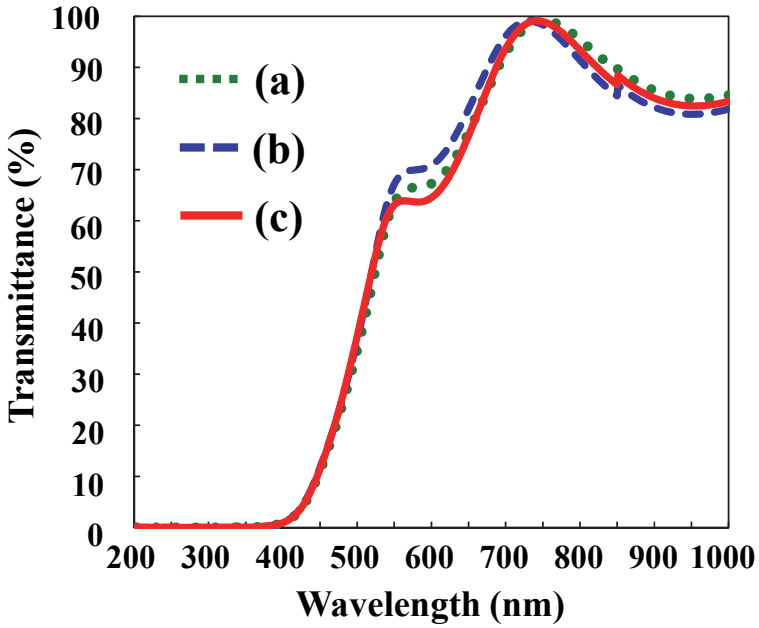

Fig. 4 (Color online) UV-visible optical transmittance spectra of (a) BF, (b) BAB, and (c) BABAB thin films prepared on MgO(100) substrates.

Fig. 4 Maruyama *et al*.

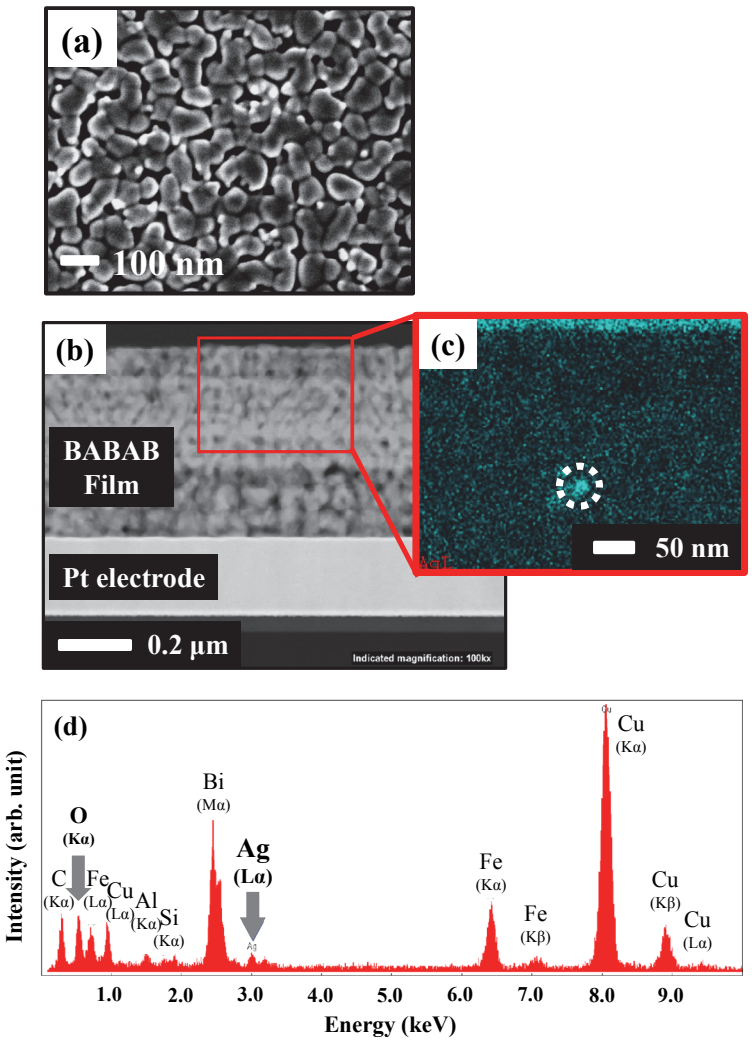

Fig. 5 (Color online) (a) FE-SEM surface image of Ag nanoparticle-coated BF thin film after heat treatment at 600°C, (b) Cross-sectional ADF-STEM image of BABAB thin film on Pt/TiO_x/SiO_2/Si substrate, (c) Ag Lα EDX signal mapping of BABAB film for selected area in (b), and (d) EDX spectrum of the circled area of BABAB film in (c).

Fig. 5 Maruyama *et al*.

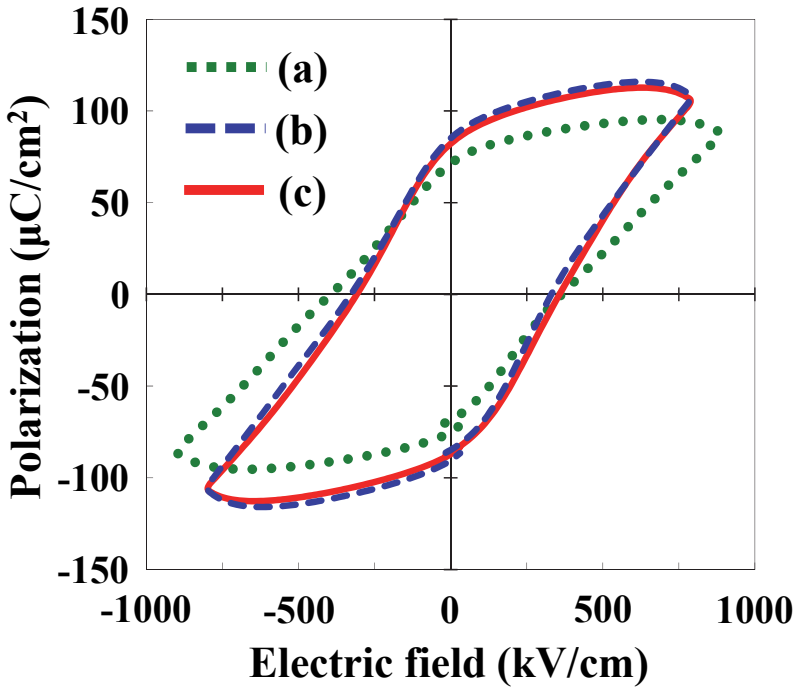

Fig. 6 (Color online) *P*–*E* hysteresis loops (measured at 83 K and 1 kHz under dark conditions) of (a) BF, (b) BAB, and (c) BABAB thin films prepared on $Pt/TiO_x/SiO_2/Si$ substrates.

Fig. 6 Maruyama *et al*.

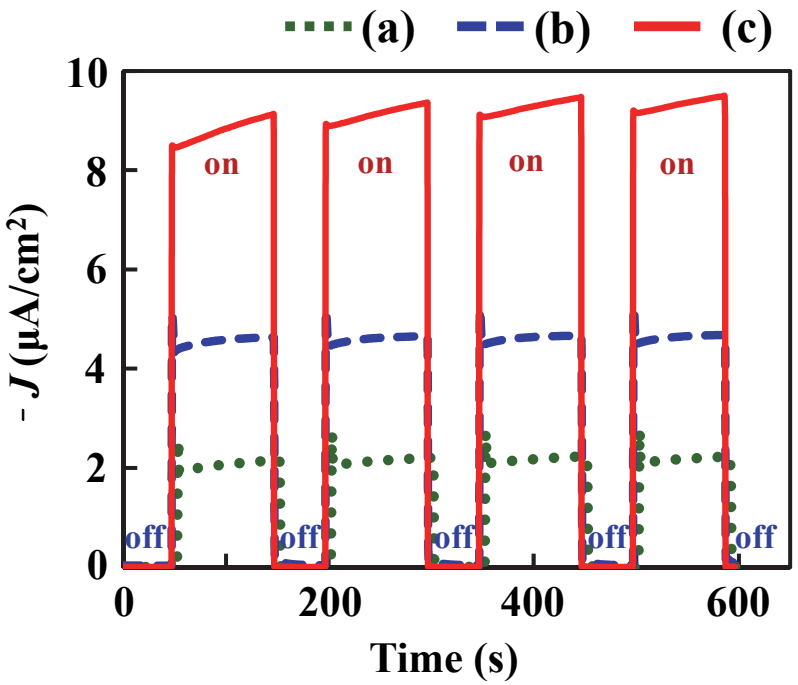

Fig. 7 (Color online) Zero-bias photoelectric current properties (measured at room temperature) of (a) BF, (b) BAB, and (c) BABAB thin films prepared on $Pt/TiO_x/SiO_2/Si$ substrates as a function of time under dark (off) and white light (λ =400–700 nm, 90 klx) irradiation (on) conditions.

Fig. 7 Maruyama *et al*.

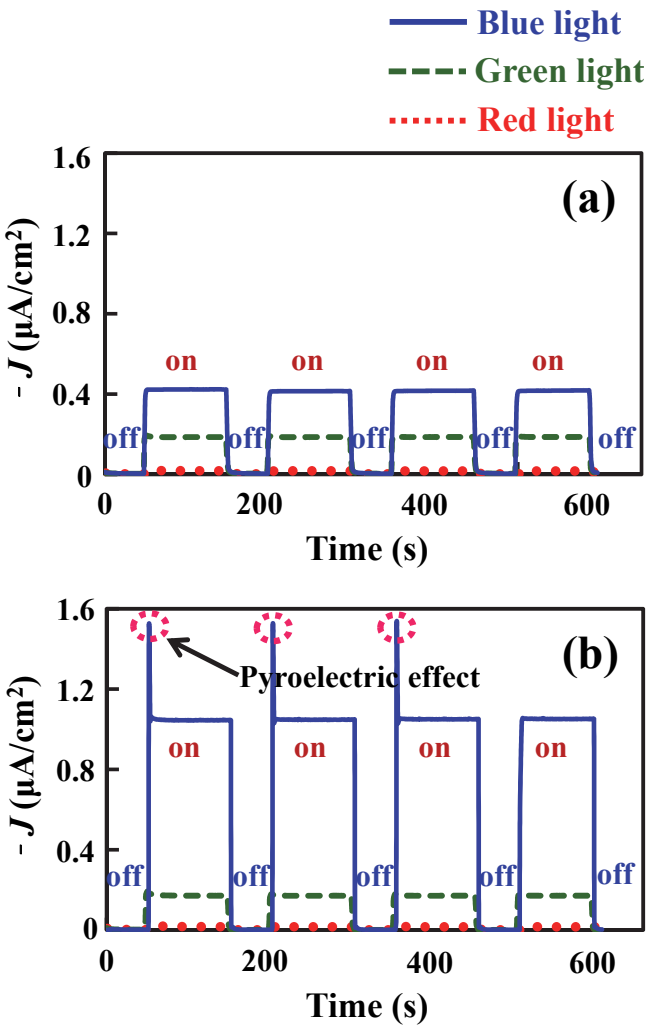

Fig. 8 (Color online) Zero-bias photoinduced current density of (a) BF and (b) BABAB thin films prepared on Pt/TiO_x/SiO_2/Si substrates as a function of time with blue light (λ = 450 nm), green light (λ = 530 nm), and red light (λ = 650 nm) on or off.

Fig. 8 Maruyama *et al*.